Slowness vector estimation over large-aperture sparse arrays with the Continuous Wavelet Transform (CWT): application to Ocean Bottom Seismometers

Roberto Cabieces,[1] Frank Krüger,[2] Araceli Garcia-Yeguas,[3] Antonio Villaseñor,[4] Elisa Buforn,[5,6] Antonio Pazos,[1] Andrés Olivar-Castaño[7] and Jaime Barco[8]

[1]*Royal Spanish Navy Observatory, Cecilio Pujazon s/n, E*-11100 *San Fernando, Spain. E-mail: rcabdia@roa.es*
[2]*Institute of Geoscience, University of Potsdam, Karl-Liebknecht-Str., 24–2514476 Potsdam-Golm, Germany*
[3]*Campus Universitario Cartuja, University of Granada, s/n,* 18011*, Granada, Spain*
[4]*Institute of Marine Sciences, Pg. Marítim de la Barceloneta,* 37–49*, E*-08003 *Barcelona, Spain*
[5]*Universidad Complutense de Madrid, Plaza de Ciencias,* 1*, Ciudad Universitaria,* 28040 *Madrid, Spain*
[6]*IGEO, Universidad Complutense de Madrid-CSIC,* 28040 *Madrid, Spain*
[7]*University of Oviedo, Geology department, Oviedo, Spain*
[8]*Instituto Geográfico Nacional, Seismology Department,* 28040 *Madrid, Spain*

SUMMARY

This work presents a new methodology designed to estimate the slowness vector in large-aperture sparse Ocean Bottom Seismometer (OBS) arrays. The Continuous Wavelet Transform (CWT) is used to convert the original incoherent traces that span a large array, into coherent impulse functions adapted to the array aperture. Subsequently, these impulse functions are beamformed in the frequency domain to estimate the slowness vector. We compare the performance of this new method with that of an alternative solution, based on the Short-/Long-Term Average algorithm and with a method based on the trace envelope, with the ability to derive a very fast detection and slowness vector estimation of seismic signal arrivals. The new array methodology has been applied to data from an OBS deployment with an aperture of 80 km and an interstation distance of about 40 km, in the vicinity of Cape Saint Vincent (SW Iberia). A set of 17 regional earthquakes with magnitudes $2 < $ mbLg $ < 5$, has been selected to test the capabilities of detecting and locating regional seismic events with the Cape Saint Vincent OBS Array. We have found that there is a good agreement between the epicentral locations obtained previously by direct search methods and those calculated using the slowness vector estimations resulting from application of the CWT technique. We show that the proposed CWT method can detect seismic signals and estimate the slowness vector from regional earthquakes with high accuracy and robustness under low signal-to-noise ratio conditions. Differences in epicentral distances applying direct search methods and the CWT technique are between 1 and 21 km with an average value of 12 km. The backazimuth differences range from 1° to 7° with an average of 1.5° for the *P* wave and ranging from 1° to 10° with an average of 3° for the *S* wave.

Key words: Wavelet transform; Computational seismology; Earthquake monitoring and test-ban treaty verification; Earthquake source observations; Seismicity and tectonics; Wave propagation.

1 INTRODUCTION

Since the early 1960s ground seismic arrays have helped to disclose Earth structures in great detail (Doornbos 1974; Goldstein *et al.* 1992; Krüger *et al.* 1993; Weber *et al.* 1996; Kito & Krüger 2001), to detect and classify nuclear explosions (Carpenter 1965; Kim & Richards 2007; Selby 2010; Gibbons & Ringdal 2012; Kværna & Ringdal 2013), to ocean microseismic analysis (Cessaro 1994; Friedrich *et al.* 1998; Behr *et al.* 2013; Reading *et al.* 2014; Gal *et al.* 2015) and more recently to track the rupture spread of big earthquakes (Ishii *et al.* 2005; Krüger & Ohrnberger 2005; Koper *et al.* 2011).

Arrays have shown a special ability to enhance the coherent signals over noise and to lower the signal detection threshold, owing to

phase alignment and signal stacking of the sensor recordings (Rost & Thomas 2002; Schweitzer *et al.* 2012; Rost & Thomas 2009). In addition, the most recent advances in marine technology let us explore seismic activity (Grevemeyer *et al.* 2017) and the acoustic wavefield through Ocean Bottom Seismometers (OBSs) and pressure sensors (Collins *et al.* 2002; Dahm *et al.* 2006; Tilmann & Dahm 2008). In this sense, the capabilities of array techniques in OBS deployments (e.g. submarine volcano exploration or earthquake location with marine foci) awaken an increased interest as well as having paramount importance in exploring the Earth's structure under the ocean bottom floor using new approaches.

However, to implement array techniques in OBS studies presents difficulties such as (i) timing errors in the array sensors (Hannemann *et al.* 2013; Le *et al.* 2018), which make it impossible to apply any array techniques to accurately estimate the apparent slowness vector, (ii) misorientation of the seismic sensor horizontal components (Stachnik *et al.* 2012; Zha *et al.* 2013) which are also important to improve the detection and to obtain an accurate slowness of *S* waves and the last significant difficulty, and (iii) the accurate ocean floor positioning (Shiobara *et al.* 1997), commonly estimated with a positioning error on the order of several tens of metres. Additional problems arise from the array technique's implementation itself, either in the frequency domain (Capon 1969) or time domain (Frankel *et al.* 1991), as it relies on high signal coherence across the array sensor records, which is generally not valid for large aperture arrays due to the degradation of the wave front caused by heterogeneities of the structure beneath the array stations, especially for high-frequency signals.

Ringdal *et al.* (1975) proposed for the first time an incoherent beamform detector, based on beamforming envelope traces instead of waveform beams and demonstrated the superiority of incoherent beamforming over conventional beamforming for regional seismic events recorded at the large aperture Norwegian Seismic Array (NORSAR). Gibbons *et al.* (2008) and Gibbons (2012) used a modified approach of incoherent beamforming based on extracting characteristic functions (CFs) from the multitaper spectrogram and also applying it to recordings from the NORSAR array. Kao & Shan (2007) implemented the source-scanning algorithm using *P*-wave envelopes to identify the earthquake's rupture plane using local network data. In the following years, these ideas have been shared with migration techniques applying shift-and-stack envelopes and CFs to locate seismic events (Gharti *et al.* 2010; Grigoli *et al.* 2013), see also Krüger *et al.* (2020) for an application to OBS data.

Earthquakes within the oceanic plate produce high-frequency Po/So guided wavetrains observable at far regional distance. These waveforms can be recorded with OBSs and usually have emergent Po onsets and frequently So onsets obscured by the Po coda (Mallick & Frazer 1990; Kennett & Furumura 2013; Shito *et al.* 2013). To build small-scale seismological arrays in the deep ocean where standard array techniques could be used is still technically challenging. Therefore Krüger *et al.* (2020) applied an incoherent beamforming technique following Grigoli *et al.* (2013) to data of an mid-aperture OBS array near the Gloria fault.

This study focuses on a new improved incoherent beamforming array technique to better overcome the problem of dealing with incoherent and noisy waveforms in large aperture arrays, based on the Continuous Wavelet Transform (CWT, Grossmann *et al.* 1989; Kumar & Foufoula-Georgiou 1997). The wavelet analysis provides a multiresolution time–frequency signal analysis, specially designed to detect transient and non-stationary signals as is the case for seismic waves (Bear & Pavlis 1997). Furthermore, the wavelet properties allow us to denoise the traces of the array from oceanic ambient

noise and to extract transient signals that preserve the phase arrival times from the characteristics of the time–frequency energy plane (i.e. CFs). The CFs will play a key role in fulfilling the coherence requirement of array techniques and will enable us to obtain the slowness vector as well as the enhancement of the oceanic phase onsets. Alternatively for comparison purposes, CFs have also been generated using the fast Short-/Long-Term Average (STA/LTA) method (Allen 1982; Grigoli *et al.* 2013), and with the help of the seismic trace envelope (Ringdal *et al.* 1975). The maxima displayed by the CFs facilitate determining with relatively high temporal resolution the oceanic Po and So wave arrivals.

The above-mentioned methods have been applied to regional data from an OBS deployment experiment carried out in the Horseshoe Abyssal Plain (HAP), SW Iberia (Fig. 1). The OBS array is placed in the HAP and it is limited in the north by the Gorringe Bank (GB), in the south by the Seine Abyssal Plain (SAP) and in the east by the Gulf of Cadiz (GC). A total of six OBSs were deployed, forming an array with an ∼ 40 km interdistance and ∼ 80 km aperture (Fig. 1). Unfortunately, one OBS (OBS04) was lost during the recovery operation.

The crustal structure of the study area is complex, presenting strong seismic velocity contrasts and gradients. Most interpretations of the GB consider it to be either an intruded mantle block or a block made of oceanic crust (Sallarès *et al.* 2013). Sallarès *et al.* (2013) modelled a seismic refraction and wide-angle reflection profile, and found a thick sediment layer in the HAP (up to 4–5 km) with *P*-wave velocities ranging from 1.5 to 3.0 km s^{-1}, and a sediment-starved GB showing much higher *P*-wave velocities ranging from 5 to 7 km s^{-1}. The basement below the sediments in the HAP shows a strong vertical velocity gradient, increasing from ∼ 3.0 to ∼ 8.0 km s^{-1} over a mere ∼ 8 km.

From a seismological point of view, the study area and the neighbouring GC are of great interest. Several geodynamic models have been proposed to explain the seismicity of the region (Carminati *et al.* 1998; Gutscher *et al.* 2002; Platt *et al.* 2003), but the structures involved in the seismic activity are still a matter of debate. So far, it has not been possible to unequivocally define the presence of a convergent boundary between Eurasia and Africa (Buforn *et al.* 2004; Grandin *et al.* 2007; Pro *et al.* 2013). Although no structure capable of generating large earthquakes has been convincingly identified, strong earthquakes have nonetheless occurred in the area. A well-known example is the earthquake of Lisbon in 1755 ($M \sim 8.5$, Gutscher 2004; Solares & Arroyo 2004), which generated a tsunami that struck the coasts of Portugal, Morocco and Spain. Moreover, in the last 40 years, three earthquakes with Mw higher than 5.0 have occurred SW of Cape St. Vincent. Pro *et al.* (2013) found that they had similar characteristics, but different rupture geometries. A key issue for solving the above-listed research problems is monitoring and location of the seismicity of this region with OBS technology. In the following, we first describe data and instruments and the characteristics of the sparse large aperture OBS array used. Then, the new methodology proposed in this study and modified standard techniques (amplitude methods, AMs, based on STA/LTA and envelope processing) are presented followed by a comparison of array-based earthquake locations with accurate network locations.

2 DATA AND INSTRUMENTS

Data were acquired from five OBSs placed 200 km SW of Cape Saint Vincent in the deep sea in 4 km water depth, operating for 8 months (2015 September–2016 April). The array has an aperture of 80 km
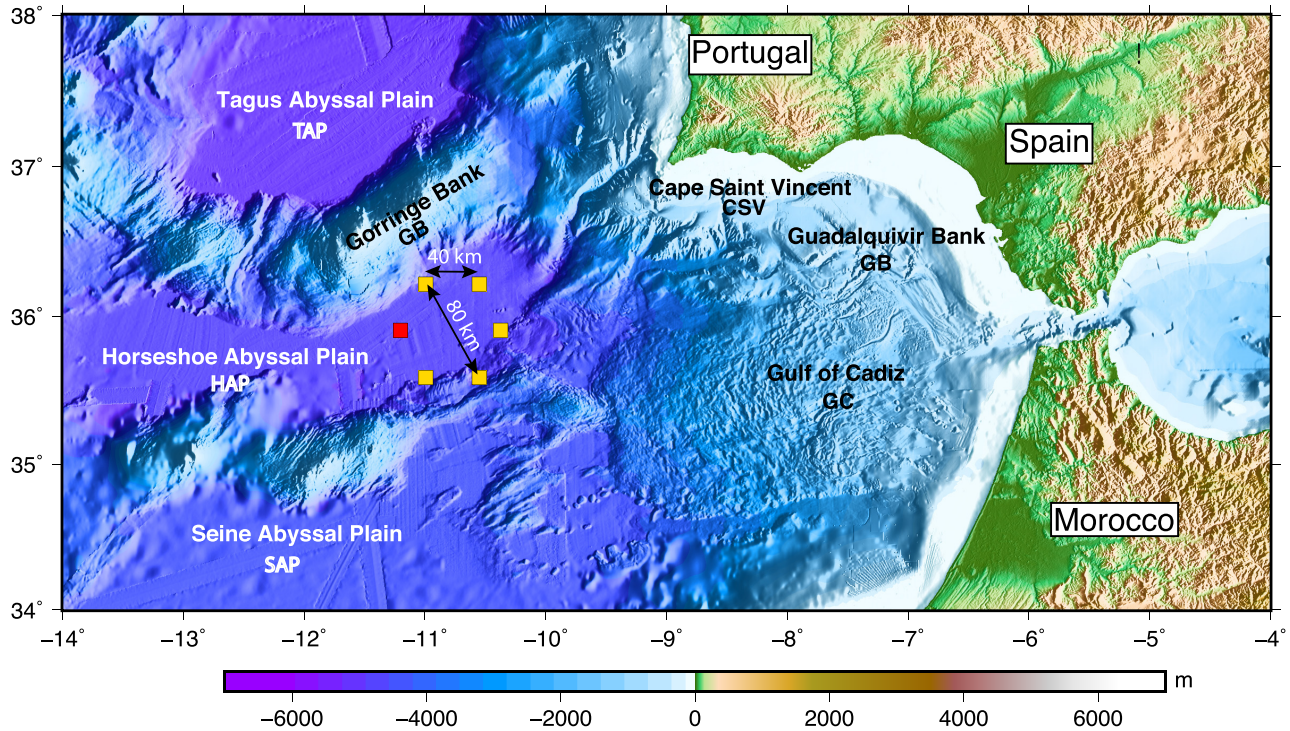
Figure 1. A geometry of the OBS array (orange squares, OBS04 red square) with a 40 km interstation distance and 80 km aperture. The array reference point is placed 200 km from Cape Saint Vincent. The bathymetry is from the General Bathymetric Chart of the Oceans (GEBCO) digital atlas (http://www.gebco.net/).

and a minimum intersensor distance of 40 km (Fig. 1). OBS 01, 02 and 03 were equipped with a three-component broad-band seismometer of type Güralp CMG-40T, with a flat response for ground velocities between 60 s—50 Hz and OBS 04 (lost), 05 and 06 were equipped with Trillium Compact, broadband seismometers with a flat instrument characteristic between 120 s—100 Hz. All OBSs have the same hydrophone (High-Tech-Inc HTI-04-PCA/ULF, flat in the range of 100 s—8 kHz). All channels were recorded with a sampling rate of 50 Hz.

The OBSs' positions were calculated using active acoustic techniques (Shiobara *et al.* 1997) and the timing errors were corrected (Supporting Information) by using the daily differences between noise cross-correlation Green's functions and a reference (Hannemann *et al.* 2013). The vertical component is realigned by a gimbaling system (Stähler *et al.* 2016) and the horizontal components of every OBS have been orientated (Supporting Information) such as to correlate the radial and the vertical components of strong Rayleigh waves from shallow teleseismic earthquakes (Stachnik *et al.* 2012; Zha *et al.* 2013). The instrument response (Scherbaum 2001; Haney *et al.* 2012) has been removed by deconvolving all of the channels to true ground velocity. For each event, the horizontal components have been rotated along the great circle arc of the seismic wave ray path, to disclose the slowness vector of the *SH* wave.

We have selected 17 regional (150 km < distance < 500 km) earthquakes with magnitudes in the range 2 < mbLg < 5, recorded during the deployment. The earthquakes selected were located (further details in Cabieces *et al.* 2020) with the non-linear location (NLL) algorithm (Lomax *et al.* 2001; Lomax *et al.* 2009) considering a flat Earth and using the first arrivals (*P* and *S* waves) in the OBSs' array recordings and in the recordings of regional on-land stations. The Earth model used to carry out the locations is a regional 3-D model (Grandin *et al.* 2007); composed by cubic cells of 1 × 1 × 1 km reaching a depth of 60 km in the region (14° W–4°

W, 34° N–38° N). The locations of the estimated epicenters have a maximum horizontal uncertainty of 13 km (size of the semimajor axis of the uncertainty ellipse, estimated at 90 per cent confidence level). These locations will be used in the following to value the accuracy of earthquake locations based on slowness vector estimates with the proposed new methodology.

3 METHODOLOGY

In this section, we first describe the characteristics of the array and its performance and then, we outline the new methodology (based on the CWT for detecting events and estimating the slowness vector) and the AMs (STA/LTA and envelope). We briefly explain the frequency-domain beamforming (BB-FK) concept and the parametrization used in the Supporting Information.

3.1 Array characteristics and performance

The array response function (ARF) which depends on the wavenumber vector ***k*** and the frequency *f,* helps to evaluate the performance of the array for a range of frequencies, given a particular wave front (Nawab *et al.* 1985; Ruigrok *et al.* 2017) and a particular array geometry configuration. A test has been carried out for different frequency bandwidths in order to analyse the performance of the array with the five remaining OBSs (e.g. Fig. 2).

The most important parameter of the array geometry is the aperture (A) of the array, in our case A = 80 km, which determines the maximum wavelength that it will be able to resolve. Note that the width of the main lobe is responsible for resolving the slowness *S*-wave front unambiguously (Fig. 2a). It is also important to estimate the frequency bandwidth in which the analysed array can attain a relatively good slowness resolution and to derive the limits
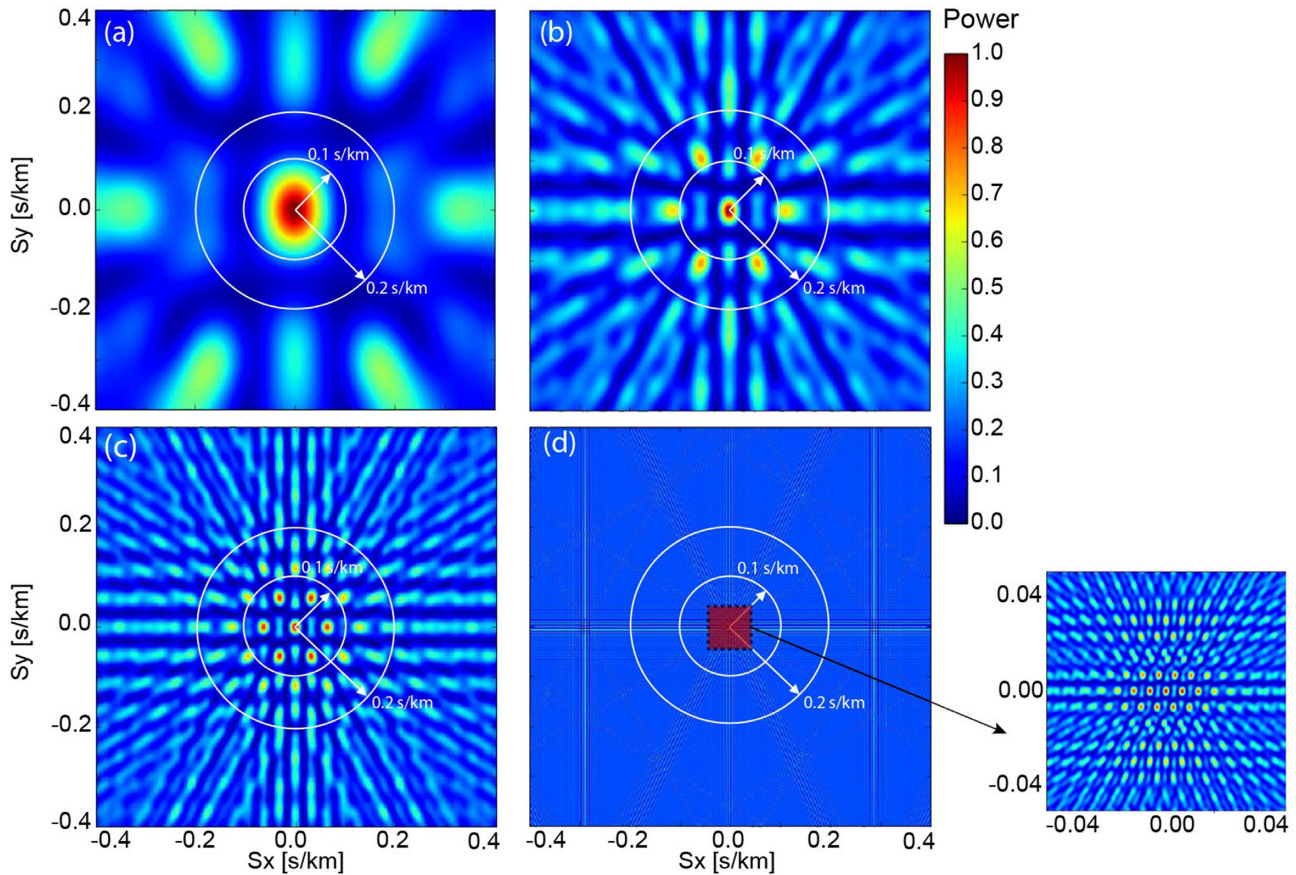
Figure 2. ARF for several frequency bandwidths. (a) ARF [0.05–0.1] Hz. (b) ARF [0.2–0.3] Hz. (c) ARF [0.4–0.5] Hz. (d) ARF [4.0–4.5] Hz. The circles show the slowness limits for teleseismic body waves (inner circle $S < 0.1$ s km^{-1}), P-waves and S-waves at regional distances ($0.1 < S < 0.2$ s km^{-1}) and $S > 0.2$ s km^{-1}.

of the maximum resolvable slowness range (increment distance in the ARF between two contiguous sidelobes), otherwise a wrong selection of the bandwidth may cause either an inaccurate estimation of the slowness vector or a solution trapped in a relative maximum of the slowness map (Figs 2b and c).

Figs 2(a) and (b) show the ARF for the frequency bands [0.05–0.1] and [0.2–0.3] Hz, respectively. In Fig. 2(a), an unambiguous main lobe is observed in contrast to Fig. 2(b) with the sidelobes near the inner ring ($S < 0.1$ s km^{-1}, the limit of the slowness for teleseismic body waves). Fig. 2(c) shows the ARF for the frequency band [0.4–0.5] Hz, slightly above the spatial aliasing limit ($f \approx 0.3$ Hz). Fig. 2(d) shows the slowness map of the ARF for the frequency band [4–4.5] Hz, which is completely saturated due to spatial aliasing.

The array configuration also plays an important role as it shapes the main lobe. In our case, the main lobe is quite similar to an ellipse with a major N-S axis orientation, which means that there is higher slowness resolution for E-W azimuths. The last important factor which is also related to the array geometry is the number of sensors, because due to more sensors there is a better ability to discriminate waves with different slowness vectors. In addition, the number of sensors determines the theoretical signal-to-noise ratio (SNR) improvement or array gain, which is proportional to the square root of the number of sensors (Rost & Thomas 2002). As a preliminary evaluation, the OBS array may be appropriate to measure the slowness of coherent teleseismic phases from any azimuth.

As shown in the ARF (Fig. 2d), the configuration of the OBS array sensors does not unambiguously discriminate slowness vectors for the frequency range of regional earthquake body waves (about 2–12 Hz). The spatial aliasing, caused by the large intersensor distances, will affect severely the slowness estimation for frequencies higher than $f \approx 0.25$ Hz (see Figs 2c and d for the frequency bands [0.4–0.5] and [4.0–4.5] Hz, respectively). On the contrary, there exists a relative narrow main lobe for low frequencies ($f < 0.25$ Hz) on the ARF, and far from ambiguous secondary lobes, shown in Figs 2(a) and (b) for the frequency bands [0.05–0.1] [0.2–0.3] Hz, respectively.

In summary, we find that even with a small number of sensors ($n = 5$), the large aperture array can analyse earthquakes with low-frequency energy content such as teleseismic phases ($f < 0.3$ Hz). However, the array is useless to detect and estimate the slowness vector from regional seismic phases because of spatial aliasing and degradation of the waveform coherence across the array, where typical dominant frequencies are in the range of 2–12 Hz.

3.2 Estimation of coherent CFs for slowness vector determination using the Continuous Wavelet Transform

The main target of the methodology presented in this paper is to find impulsive functions that represent the incoming wave onset and preserve its similarity in the frequency bandwidth in which we can apply the beamforming procedure. These CFs are simply a representation of the actual arrival times of the seismic phases
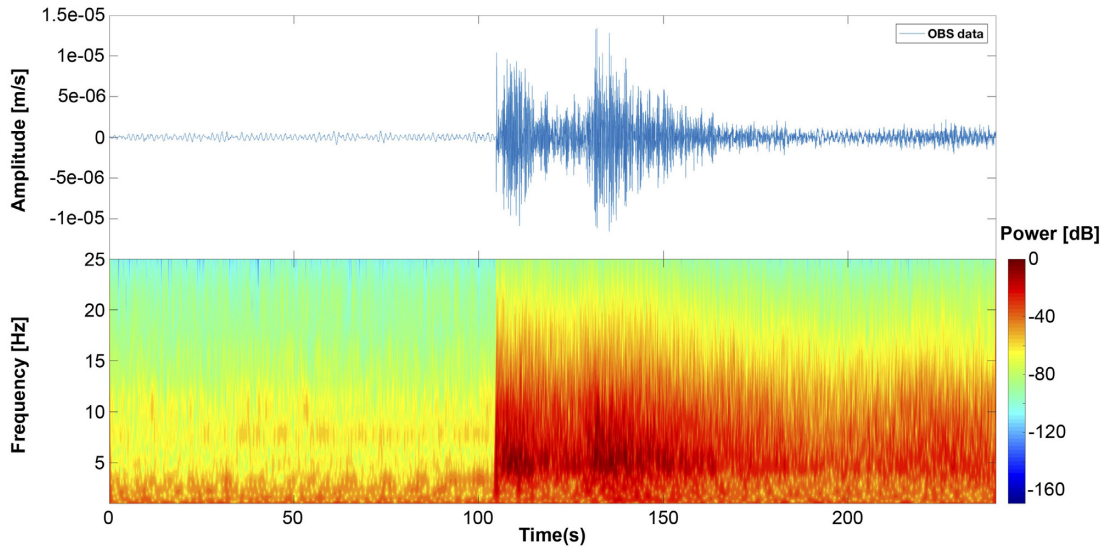
Figure 3. Scalogram ($w = 5$–8 cycles), estimated from the vertical component recorded at OBS05 station for a regional earthquake (T16, Table 1).

that facilitate the determination of the slowness vector, especially for arrays with few sensors. Furthermore, the use of CFs can help improve the detection of the phase arrival times for events with very low SNR and/or emergent onset, especially in automatic processing of large data sets.

This methodology will be focused on deriving the CFs through the common characteristics and similarity of patterns in the power density time–frequency plane by a wavelet transform analysis. The complex nature of the seismic waveforms, which are transient non-stationary signals, makes it difficult to extract the true power density. Wavelet Transform is a well-proven tool to analyse the evolution of the frequency content as a function of time (Daubechies & Bates 1992; Mallat 2009),

In order to estimate a correct CF, we need a wavelet transform with the ability to separate instantaneous frequencies as well as time resolution to provide a sufficient time-varying signal change. We use a quasi-analytic wavelet $\psi(t)$ (being the Fourier Transform $\hat{\psi}(f) \approx 0$ for $f < 0$); more precisely, the normalized Morlet wavelet defined as,

$$\psi(t) = \frac{1}{(\sigma_t^2 \pi)^{1/4}} e^{-\frac{t^2}{2\sigma_t^2}} e^{i2\pi f_c t} \tag{1}$$

where

$$\sigma_t = \frac{w}{2\pi f_c} \tag{2}$$

here f_c, is the center frequency of the Morlet wavelet, w the number of cycles and σ_t the scale of the Morlet wavelet. The Morlet wavelet (eq. 1) is a complex sine wave modulated by a Gaussian function. A complex wavelet is chosen due to its ability to accurately analyse oscillatory signals, such as seismic waves, preserving the magnitude and the phase information (Bayram 2013). On the other hand, the dilatation of the wavelet is managed by the number of cycles (w), and it is related to the scale factor σ_t (width of the Gaussian function) by eq. (2).

The number of cycles is set to control the trade-off between temporal and frequency resolution by defining the width of the Gaussian time window. In Fig. 3, we show the scalogram for the vertical component of an earthquake of magnitude $m_{bLg} = 4.0$ and at an epicentral distance of 230 km recorded at OBS05. The scalogram (Rioul & Flandin 1992) has been estimated for the frequency band

[1–25] Hz increasing the number of cycles from 5 to 8 (further details of parameter settings in the Supporting Information). We observe that the scalogram highlights the *P*-wave phase arrival as a maximum of energy between [2–8] Hz and the arrival of the *S* wave in the frequency band [2–12] Hz.

Afterwards, we find the CFs by calculating the logarithmic differences between contiguous components of the scalogram along the time axis in the frequency range of interest and then stacking those differences to obtain a time-domain function, $A(t)$. This is done following

$$A(t) = \frac{1}{n} \sum_{f=f_o}^{fn} \{\log(P_w f(t+1, f)) - \log(P_w f(t, f))\} \tag{3}$$

here, n is the number of samples and f_o, f_n are the lower and the upper frequency limits of interest and $P_w f$ is the scalogram (i.e. $P_w f(t, f) < 1$ after deconvolving to true ground velocity). Taking the logarithmic differences is a simple way to decrease the dynamic range of the scalogram components.

On the one hand, the stack is needed to reduce the loss of power information for the higher frequencies due to the shape of the scalogram and on the other hand, because a non-orthogonal wavelet analysis such as is used in this study is highly redundant at large scales, it may cause imprecision in power estimations for high frequencies. Finally, we simply filter every $A(t)$ with a zero-phase low-pass filter to obtain the CFs. This smoothing will let us find a function with an energy content adapted to our array and also to produce CF coherence.

An example of the smoothing effect is shown in Fig. 4. Data corresponding to the record of Earthquake T16 (Table 1) from the vertical component of the OBS02 are displayed at the top (Fig. 4a) for a 250-s wide time window. The bottom of Fig. 4 displays the CFs which are derived after filtering $A(t)$ with an order 3 zero-phase Butterworth low-pass filter for three different corner frequencies, where the red CF was low-passed filtered using a corner frequency of 0.05 Hz, the green CF of 0.1 Hz and the yellow CF of 0.15 Hz, respectively.

The process to obtain the CFs removes all the phase information but allows reliable determination of the phase arrival time and
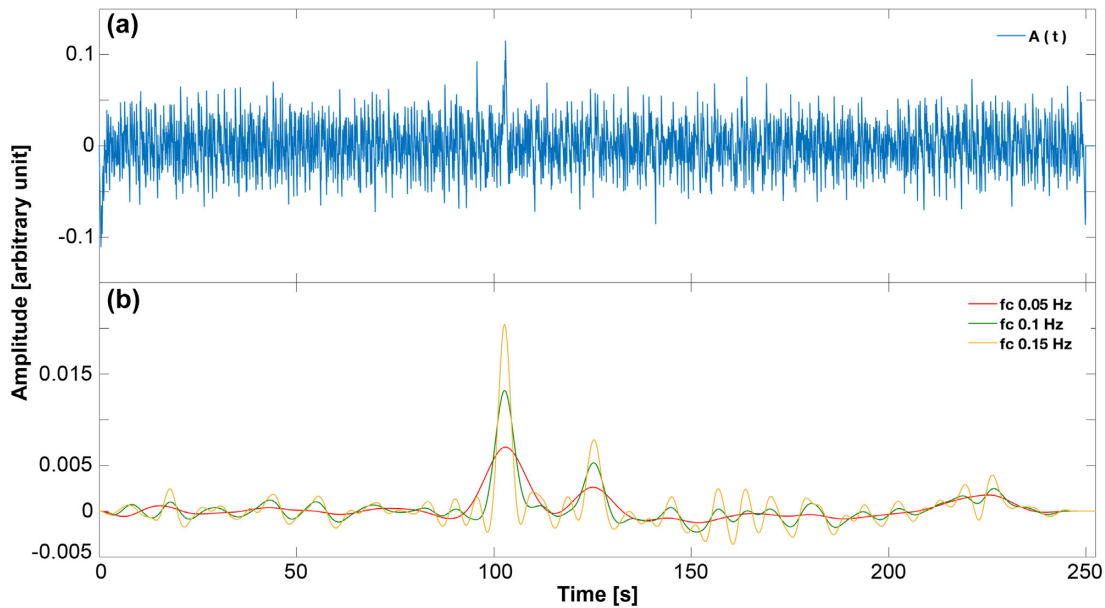
Figure 4. Example of CWT method application to the vertical component of station OBS02, for Event T16 (see Table 1). (a) Raw $A(t)$ function. (b) The corresponding CF, after application of different low-pass filters with corner frequencies of 0.05, 0.1 and 0.15 Hz.

derives surrogate waveforms in the frequency bandwidth in which spatial aliasing can be avoided in subsequent beamforming.

Fig. 5 summarizes the process of deriving the CFs from the CWT technique implemented for Earthquake T1 (Table 1). Fig. 5 (right-hand panels) show the scalograms computed for the bandwidth [2–12] Hz with a constant number of cycles set to eight. The seismograms of the OBS array are displayed together with the underlying CFs in Fig. 5 (left-hand panels). The waveforms are incoherent from site to site in the array, however the scalograms are more uniform, which helps to build coherent CFs. The CFs display relative maximum values at the times of the phase arrivals as well as an energy content suitable to facilitate the beamforming process to estimate the slowness vector. All in all, the CWT methodology will permit the exploitation of the similarity of scalograms among the sensor's array to avoid relying on the underlying coherence of waveforms.

3.3 Amplitude methods

As we mentioned before, we are trying to detect earthquake signals and then estimate the slowness vector, transforming the original raw seismograms into CFs. Implementing the CWT method, we find relatively accurate (the peaks of CFs approximate the phase arrival time with relative low uncertainty), reliable, and well-defined CFs (Fig. 5). However, for comparison and to test a faster scheme to estimate the CFs, we follow Grigoli *et al.* (2013) and Krüger *et al.* (2020) that took advantage of the classical STA/LTA method to get a primary detection of the event and a very fast slowness vector estimation.

The STA/LTA ratio of the signal y, is derived by,

$$\text{STA} = \frac{1}{N_s} \sum_{n=1}^{N_s} y_n, \tag{4}$$

and

$$\text{LTA} = \frac{1}{N_L} \sum_{n=-N_L}^{0} y_n. \tag{5}$$

Where N_s, is the number of samples in the STA time window [1 N_s] and N_L is the number of samples in the LTA time window [$-N_L$ 0].

The process to calculate the CFs by the STA/LTA, (Figs 6d and e), starts applying a high-pass filter to the signal to clean it of low-frequency noise and to calculate the STA/LTA. The STA works by measuring the 'instant' amplitude of the seismic signal (Trnkoczy 2012), while the LTA takes care of average seismic noise. This strategy permits us to determine the precise instant of the incoming abrupt energy change from the wave front. Finally, the temporal traces obtained from the ratio STA/LTA are filtered with a low-pass filter to estimate the smooth time-varying power of the signal, CF.

In parallel, the envelope of the seismic traces $|H(t)|$ can be calculated from the analytic signal (Oppenheim & Schafer 2010),

$$H(t) = y(t) + i y_h(t) \tag{6}$$

where $y_h(t)$ is the Hilbert transform of the trace, $y(t)$. We compute the envelope using the Python seismology toolbox ObsPy (Beyreuther *et al.* 2010).

The envelope (Figs 6b and c) slowly follows the signal energy changes and is stable enough to build CFs. In this sense, the analytic signal behaves like the CWT with a complex wavelet (Bruns 2004). Both slowly follow the energy signal content and preserve the phase information (Bear & Pavlis 1997). Finally, the envelope is also filtered with a low-pass filter in order to obtain CFs. An example of this technique is shown in Fig. 6, which summarizes all the stages of the technique. First, we have filtered the vertical component of Earthquake T4 (Table 1) recorded at OBS01 (Figs 6a and c) by applying a high-pass filter ($f_c = 0.5$ Hz) to remove low-frequency noise and to take into account the previous estimated power spectrum of the signal. The envelope of the seismic trace (red line) is derived from the analytic signal and is shown in Fig. 6(c) together with the seismic signal (blue line). Then, the envelope is filtered (low-pass $f_c = 0.15$ Hz) in Fig. 6(d) to obtain the CFs. On the other hand, the STA/LTA time function is displayed in Fig. 6(a) (red line). The STA/LTA time function is filtered using a low-pass filter at 0.15 Hz (Fig. 6b) to obtain the matching CF. Both of the CFs, the envelope

(Fig. 6d), and the STA/LTA (Fig. 6b) are similar and they softly represent the *P*- and *S*-wave onsets. In this example, the *S*-wave onset is represented by the CF which has a larger amplitude than the *P*-wave onset in the CF, as the SNR of the *S* wave is higher than that of the *P* wave (typical feature in the oceanic waves Po/So).

3.4 Epicentre determination from CFs

The epicentre determinations by the OBS array are obtained using the backazimuth (BAZ) that corresponds to the maximum power of the optimal slowness vector and the distance between the array reference point and the estimated epicentre. The distance is calculated by,

$$D = \frac{\Delta t_{s-p} V_s V_p}{V_p - V_s} \tag{7}$$

where Δt_{s-p} is the difference of the arrival times for the *P* and *S* waves retrieved from the beam of the CFs for the optimal *P*/*S* slowness vector and V_p, V_s are the mean velocity values of the *P* and *S* waves in the oceanic crust and upper mantle (up to 50 km

depth). In this paper, we have estimated $V_s \sim 4.087 \, \text{km s}^{-1}$ and $V_p \sim 7.078 \, \text{km s}^{-1}$ according to a 3-D model (Grandin *et al.* 2007), averaging the velocity of the 3-D model grid cells in layers of 1 km depth in the region 14° W–5° W and 34° N–38° N, and then calculating the mean of the velocity layers.

4 RESULTS

The methodology has been tested by comparing epicenters derived from the CWT methodology with a set of regional earthquakes that took place during the array survey and were located (Cabieces *et al.* 2020) with the NLL method (Lomax *et al.* 2009) and using the 3-D model of Grandin *et al.* (2007). Table 1 shows the numerical results of locations (E1, CWT Array method and E2, NLL method) along with the BAZ and slowness with their uncertainties calculated from the tangents to the main lobe of the slowness map at 5 per cent below the maximum power. For comparison, we also show the slowness vectors estimated with the AM (Table 2), although only $\sim$ 50 per cent of the Po onsets of the selected earthquakes could be detected

Table 1. Results from the slowness vector estimation and the array epicentre determination (using the CWT). E1, hypocentre estimation from the seismic network. E2, epicentre estimation from the array. Dist Array corresponds to the distance from the array reference to E2. BAZ$_{P,S}$ is the backazimuth derived from the slowness vector. BAZ$_{P,S}$ difference is the difference between the backazimuth of the great circle arc (from the array reference to E1) and the backazimuth that is derived from the slowness vector. S_P difference is the difference between the empirical slowness and the slowness that is derived from the slowness vector. $|S_{P,S}|$, is the slowness absolute value. ΔBAZ and ΔS are the errors associated with the backazimuth and the slowness when the maximum power decreases by 5 per cent.

Earthquake	To	Magnitude (mbLg)	E1 Lat Lon	E2 Lat Lon	Depth (km)	Dist Array (km)	Dist |E1−E2| (km)	BAZ$_{P,S}$ ±ΔBAZ (o)	BAZ$_{P,S}$ difference (o)	$\|S_{P,S}\|$ ±$\Delta S_{P,S}$ (s km^{-1})	S_P difference (s km^{-1})
T1	17-09-2015 15:11:45.02	5.0	35.71 −7.03	35.59 −7.05	36 ± 8	332	13.1	97 ± 1 100 ± 1	4 7	0.11 ± 0.01 0.22 ± 0.02	− 0.012
T2	28-09-2015 07:25:09.13	4.5	34.70 −11.87	34.65 −11.79	58 ± 2	172	9.5	215 ± 2 218 ± 3	−4 0	0.13 ± 0.01 0.21 ± 0.01	0.011
T3	28-09-2015 17:03:40.24	2.3	36.14 −7.96	36.02 −7.97	48 ± 15	248	13.3	86 ± 4 92 ± 4	3 8	0.12 ± 0.03 0.21 ± 0.04	0.016
T4	20-10-2015 20:15:25.44	4.7	35.81 −5.73	35.81 −5.96	27 ± 9	449	21.0	91 ± 2 100 ± 2	0 10	0.12 ± 0.02 0.19 ± 0.02	− 0.003
T5	21-10-205 8:39:58.80	3.0	37.23 −8.54	37.23 −8.56	22 ± 1	243	2.0	51 ± 2 49 ± 2	−1 −4	0.12 ± 0.02 0.20 ± 0.02	0.002
T6	24-10-2015 20:31:17.00	2.4	36.53 −11.54	36.59 −11.61	43 ± 10	103	10.0	314 ± 3 309 ± 2	2 − 3	0.12 ± 0.02 0.21 ± 0.02	0.005
T7	07-11-2015 18:11:58.27	4.0	36.68 −5.47	36.44 −5.62	18 ± 15	472	14.5	84 ± 2 81 ± 2	6 3	0.12 ± 0.01 0.19 ± 0.02	0.032
T8	18-11-2015 13:13:15.24	3.0	36.80 −7.17	36.87 −7.29	31 ± 3	332	13.7	69 ± 2 77 ± 2	−3 5	0.11 ± 0.02 0.19 ± 0.02	0.014
T9	19-11-2015 21:57:02.71	3.2	36.90 −8.92	36.96 −8.92	37 ± 2	187	11.4	53 ± 2 60 ± 1	−2 4	0.12 ± 0.01 0.19 ± 0.01	0.024
T10	01-12-2015 11:09:59.89	4.5	36.95 −12.08	36.94 −12.06	58 ± 11	171	2.7	312 ± 2 310 ± 2	0 −3	0.11 ± 0.01 0.22 ± 0.02	− 0.028
T11	06-12-2015 22:17:42.06	3.5	35.34 −6.17	35.28 −6.14	0.5 ± 14	414	7.9	98 ± 3 106 ± 3	1 8	0.12 ± 0.01 0.18 ± 0.02	− 0.009
T12	21-12-2015 02:17:04.81	4.2	36.80 −13.18	36.89 −12.89	58 ± 13	244	28.0	301 ± 2 285 ± 2	7 − 9	0.10 ± 0.01 0.21 ± 0.01	− 0.017
T13	31-12-2015 20:04:39.78	2.9	36.55 −7.26	36.61 −7.40	15 ± 2	317	14.4	80 ± 2 82 ± 2	4 6	0.12 ± 0.02 0.20 ± 0.02	0.034
T14	09-01-2016 06:25:30.09	4.7	36.15 −12.69	36.19 −12.67	48 ± 17	182	12.6	284 ± 2 279 ± 2	5 1	0.10 ± 0.02 0.20 ± 0.02	− 0.019
T15	25-02-2016 01:03:24.02	2.8	34.89 −5.18	34.80 −5.15	2 ± 2	513	10.5	98 ± 2 108 + 2	−3 7	0.13 ± 0.02 0.21 ± 0.02	− 0.018
T16	02-03-2016 13:41:11.68	4.0	36.22 −8.16	36.23 −8.05	45 ± 10	231	10.3	83 ± 2 87 ± 2	2 6	0.12 ± 0.02 0.20 ± 0.02	0.007
T17	07-03-2016 12:33:18.98	3.9	35.50 −5.11	35.36 −5.10	15 ± 18	507	15.8	97 ± 4 99 ± 5	4 5	0.11 ± 0.03 0.20 ± 0.04	− 0.018
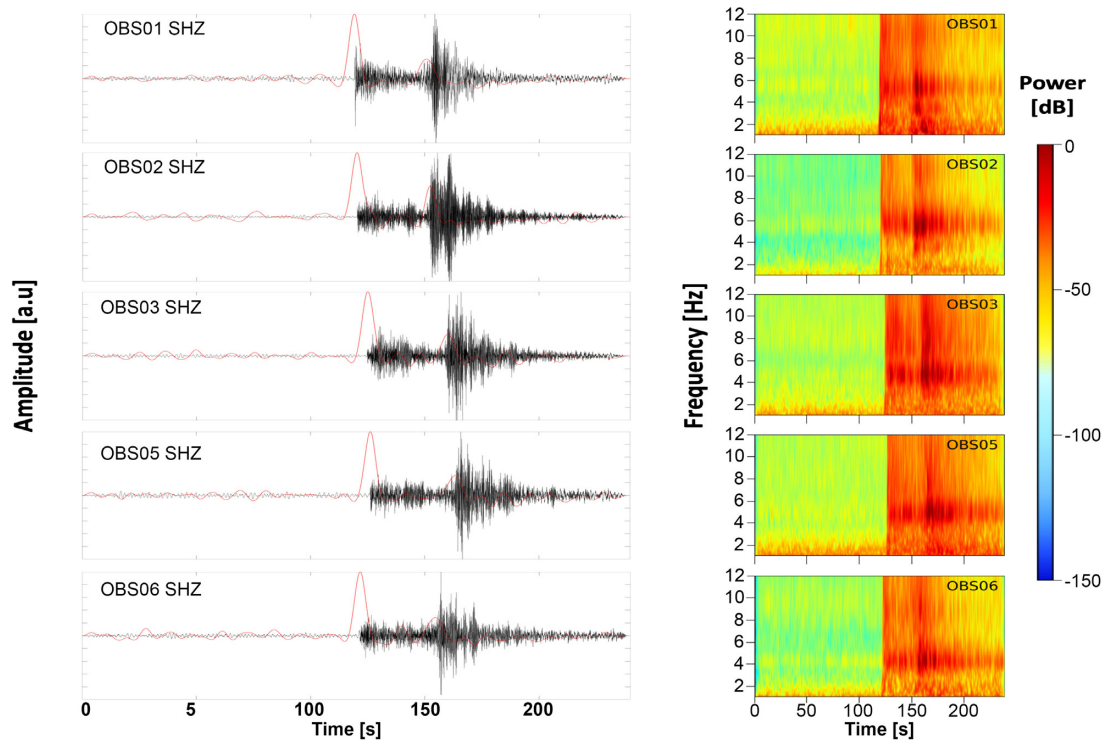
Figure 5. The left-hand panels correspond to the seismograms (black line, normalized amplitude and high-pass filtered $f_c = 0.5$ Hz) for every OBS (vertical component) in the array and the CFs (red line, normalized amplitude, and low-pass filtered functions $A(t)$ with $f_c = 0.15$ Hz). The right-hand panels correspond to the scalograms computed from the seismograms ($w = 8$) of the Earthquake T1 (see Table 1).
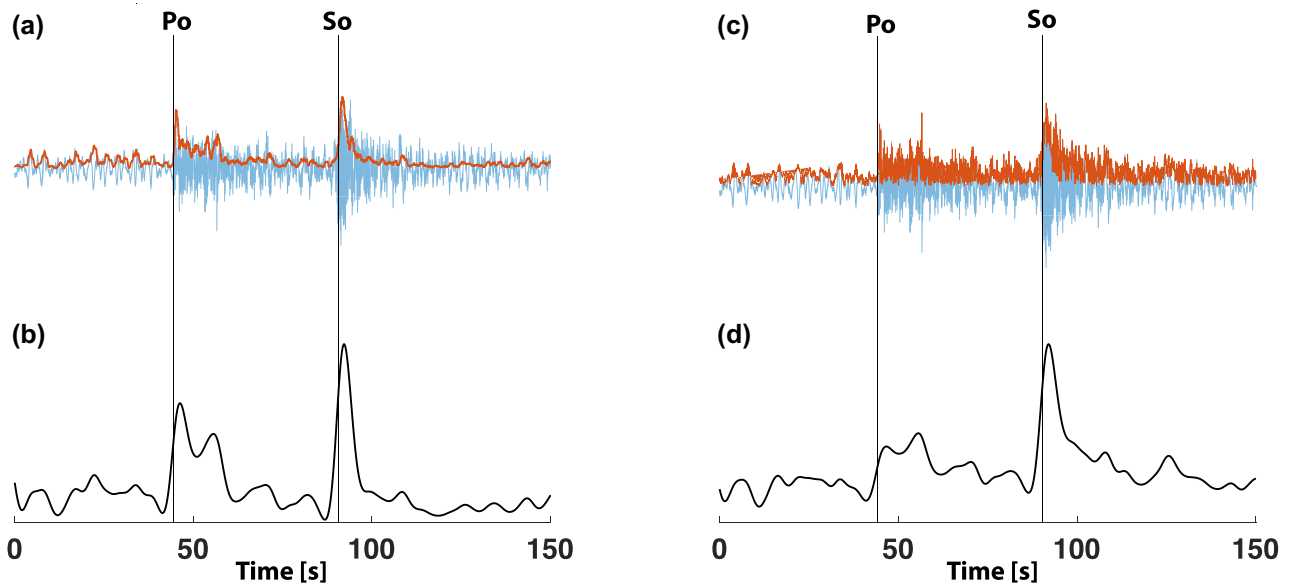
Figure 6. AM application, vertical component of station OBS01 and Event T4 (see Table 1). (a) Seismic trace (blue colour) and STA/LTA time function (red colour). (b) CF, Filtered STA/LTA time function (low-pass filtered $f_c = 0.15$ Hz). (c) Seismic trace (blue colour) and Envelope of the seismic trace (red colour). (d) CF, Filtered Envelope (low-pass filtered $f_c = 0.15$ Hz). The seismic trace has been pre-filtered with a zero-phase high-pass filter (f_c 0.5 Hz) of order 3.

using the AM. In those cases in which the Po is missed, the location of the earthquake based on the slowness vector and the So−Po difference time was not possible. Also note that while the Po of some earthquakes is missed, the So is still detected.

The set of epicentres located with NLL is the reference to evaluate the accuracy and possible deviations of the BAZ and slowness determined by the CWT array methodology. These earthquakes

were selected to cover many different azimuths, magnitudes [2.0–5.0] m_{bLg} and epicentre distances. The epicentre distances ranged from 150 to 500 km from the array centre, keeping in mind that because of the plane wave front assumption, we can only estimate the slowness vectors of epicentre distances from more than two times the array aperture (Almendros *et al.* 1999). In Fig. 7, the epicentres determined by the OBS array (red circles) are shown

Table 2. Results comparison between CWT and AM. BAZ_T backazimuth of the great circle arc, and S_{EP} empirical slowness of the *P* wave. $BAZ_{P,S}$ is the backazimuth derived from the slowness vector. $|S_{P,S}|$, is the slowness absolute value. Empty fields stands for not detected phase.

Earthquake	BAZ_T	$BAZ_{P,S}$ CWT (o)	$BAZ_{P,S}$ STA/LTA (o)	$BAZ_{P,S}$ Envelope (o)	S_{EP}	$|S_{P,S}|$ CWT (s km^{-1})	$|S_{P,S}|$ STA/LTA (s km^{-1})	$|S_{P,S}|$ Envelope (s km^{-1})
T1	101	97	91	90	0.10	0.11	0.12	0.12
		100	100	98		0.22	0.19	0.17
T2	211	215	–	–	0.14	0.13	–	–
		218	214	212		0.21	0.23	0.19
T3	89	86	–	–	0.14	0.12	–	–
		92	–	91		0.21	–	0.24
T4	91	91	114	115	0.12	0.12	0.13	0.10
		100	92	94			0.19	0.17
T5	50	51	–	–	0.12	0.12	–	–
		49	44	37		0.20	0.17	0.18
T6	316	314	–	–	0.12	0.12	–	–
		309	301	306		0.21	0.20	0.19
T7	90	84	–	–	0.15	0.12	–	–
		81	77	68		0.19	0.18	0.17
T8	66	69	–	–	0.12	0.11	–	–
		77	–	–		0.19	–	–
T9	51	53	44	45	0.15	0.12	0.11	0.10
		60	49	52		0.19	0.17	0.16
T10	312	312	–	–	0.10	0.11	–	–
		310	308	306		0.22	0.20	0.19
T11	99	98	92	88	0.10	0.12	0.12	0.12
		106	100	99		0.18	0.19	0.17
T12	308	301	288	–	0.10	0.10	0.13	–
		285	275	274		0.21	0.23	0.19
T13	84	80	81	86	0.15	0.12	0.15	0.15
		82	75	81		0.20	0.20	0.19
T14	289	284	–	–	0.10	0.10	–	–
		279	–	–		0.20	–	–
T15	95	98	110	114	0.11	0.13	0.130	0.11
		108	–	–		0.21	–	–
T16	85	83	79	81	0.13	0.12	0.12	0.11
		87	79	78		0.20	0.18	0.17
T17	101	97	92	87	0.10	0.11	0.10	0.09
		99	100	100		0.20	0.17	0.17

together with the set of selected epicentres (grey circles) and its uncertainty horizontal ellipses (grey ellipses). The minimum distance between E1 and E2 is 1 km, the maximum is 21 km and the mean is 12 km (excluding the anomalous results of Earthquakes T7 and T12).

Fig. 8 is a polar representation centered on the array, intended to better visualize the BAZ difference between the BAZ of solution E1 and E2 (Table 1, BAZ difference). The BAZ difference is highlighted in a colour scale showing the range of values for the *P* wave on the left and *S* wave on the right-hand side. The symbol size is proportional to the apparent slowness, with values from 0.11 to 0.13 s km^{-1} for *P* waves and 0.18 to 0.22 s km^{-1} for *S* waves.

BAZ difference values for the *P* wave tend to be slightly lower than those for the *S* wave with a maximum for the *P* wave of 7° and a maximum for the *S* wave of 10°. Both of them have the same tendency toward positive differences and even sharpen for the *S* wave in the angular sector [60°–120°]. The other angular sector with high azimuth deviation is the sector between [270°–330°] deg. The overall results in the BAZ difference are a mean value of a

1.5° for the *P* wave with a standard deviation of 3.0° and for the *S* wave of 3.0° with a standard deviation of 5.0°, respectively. For the detected earthquakes by the AM (Table 2), the mean of the BAZ differences are significantly higher than the CWT with 11.0° and 7.2° for the *P* and *S* waves, respectively using the STA/LTA and with a mean of 11.5° and 7.5° using the envelope.

5 DISCUSSION

The CWT application herein shows that it is possible to detect the seismic signal and determine with good precision the slowness vector from regional earthquakes as seen in the results section (Table 1). First, we briefly discuss the efficiency of the CWT methodology over the conventional BB-FK array technique (BB-FK implementation details in the Supporting Information) outlining the most important features and then we compare the CWT method with the AM.

In Figs 9(b) and (c), we show the semblance coefficient for a sliding time window (24 s) using the unfiltered seismic signal beam
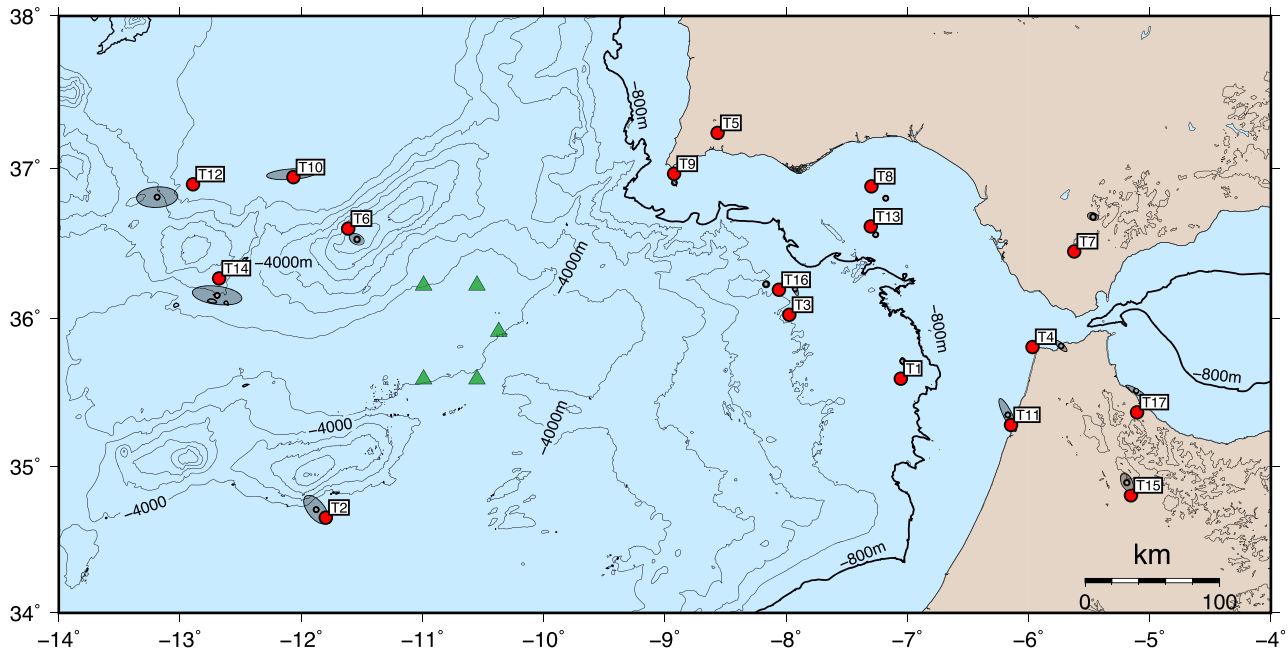
Figure 7. Distribution of epicentres located using the CWT methodology (red circles). Epicentre locations derived from the seismic network using the NLL method (black circles) and horizontal uncertainty ellipses (grey ellipses—length of the ellipse axes is multiplied by a factor of 2). OBS Array (green triangles).
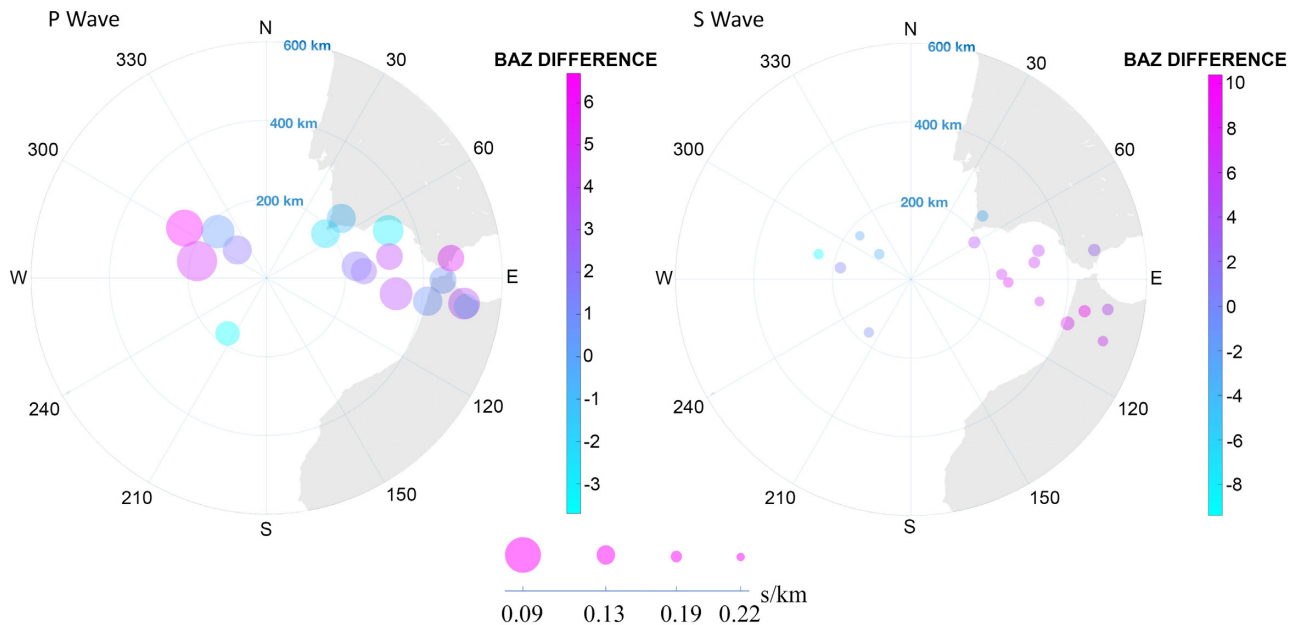

Figure 8. Left: *P* wave and right: *S*-wave polar bubble plot. The radius is the distance from the array centre. The colour gradient compares the BAZ derived from the array and the BAZ toward the event (great circle arc) for each earthquake's epicentre. The circle size is proportional to the apparent velocity of the phase [0.09–0.22] s km^{-1}.

of Earthquake T9 (Table 1). It is not a surprise that no stable solution is found for the slowness or BAZ in the typical frequency seismic bandwidth [5.5–6.5] Hz using BB-FK. Fig. 9 summarizes both difficulties, the spatial aliasing problem and the impossibility of finding a reliable beam power from incoherent traces. Next, we compute the BB-FK for the same earthquake but using sliding windows (24 s, bandwidth [0.05–0.1] Hz) from the CFs obtained with the CWT method (Fig. 9d) to derive a stable and reliable solution for the slowness and BAZ (Figs 9e and f). Fig. 9(d)

displays how the Po and So onset is detected in the CFs' beam (red line).

In Figs 10 and 11, we focus on the differences and limitations between the AMs and the CWT with the help of the T2 earthquake example. Previous to the computation of the AMs and CFs, we applied a zero-phase high-pass filter ($f_c = 0.5$ Hz) to the raw seismic signals intended to remove the oceanic seismic noise. Moreover, the CWT is applied in the bandwidth [0.5–25] Hz to be able to compare both methodologies and to take into account the power spectrum of
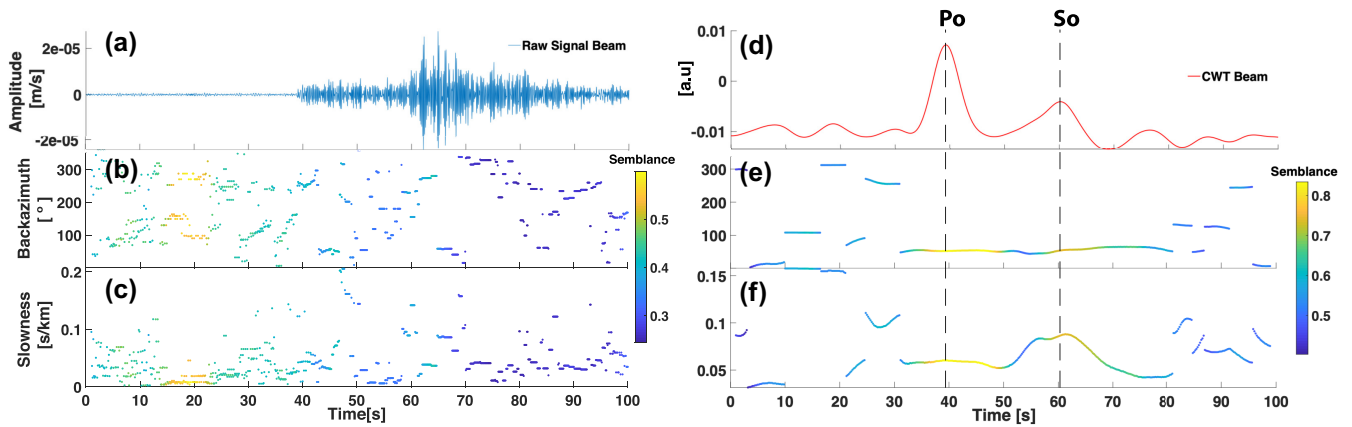
Figure 9. BB-FK analysis of Earthquake T9, vertical component. (a) Beamforming of the five OBS raw traces. (b) BAZ according to the maximum semblance inside a sliding time window (22 s) for the entire analysis period (100 s). (c) Like (b) but for slowness. (d)–(f) show the BB-FK using the CFs derived from the CWT methodology.
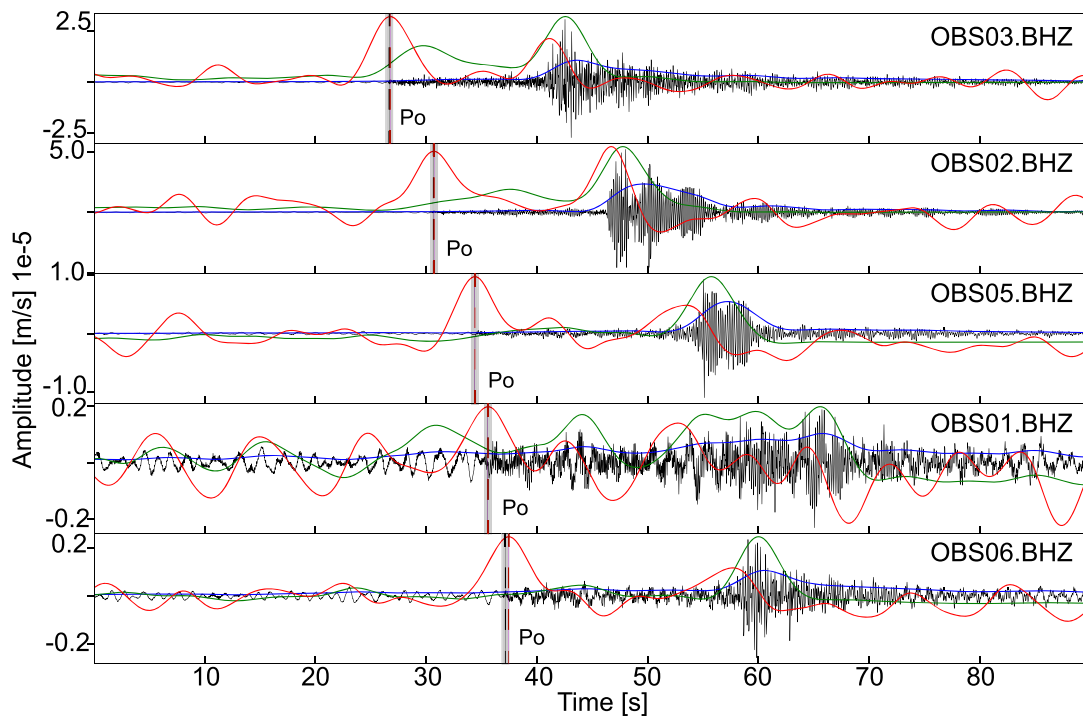

Figure 10. Detection of the Po in the OBSs array vertical component. Red line is the CFs built from the CWT, green line CFs built from the STA/LTA and blue line CFs built from the envelope. The seismograms has been filtered with a high-pass filter ($f_c = 0.5$). Shadow areas are the errors bar associated with the manual picked Po.

the T2 earthquake. The parameters of the CWT and AM method are not optimized for this test, we simply use the common parameters (see parameter settings section in the Supporting Information) $\omega_o = 8$ in the CWT and the ratio of the STA/LTA window length to 1/40.

As mentioned in Section 3, the AM was designed to very quickly detect the seismic signal and to retrieve a primary estimation of the slowness vector. But occasionally, some earthquake first arrivals cannot be detected or its detection is greatly delayed by the STA/LTA algorithm or by the envelope with low SNR conditions (Fig. 10). Nevertheless, thanks to the convolution narrow filter effect, the CWT can very accurately extract the CFs from the seismic energy with low SNR and it also allows the detection of transients in signals

with diffuse energy over a wide frequency band. Fig. 10 shows the detection comparison between the CWT and the AM methods, where it is remarkable that while the maxims displayed (red picks) by the CWT CFs are in agreement with the manual picks (black picks), the AM methods (green line the STA/LTA and blue line the envelope) are not able to detect the emergent arrival of the Po.

In Fig. 11, we display the CFs' beam retrieved from the CWT and the AM methods, together with the slowness maps for the Po and So waves. The CF beam of the Po and So waves show clear maxims when using the CWT (Fig. 11a), but the Po is not detected by the AM method. It is also remarkable in the example we are analysing that the So-wave detection is delayed in the AM (Figs 11b and c). This delay is likely caused by the contamination of the S_o wave
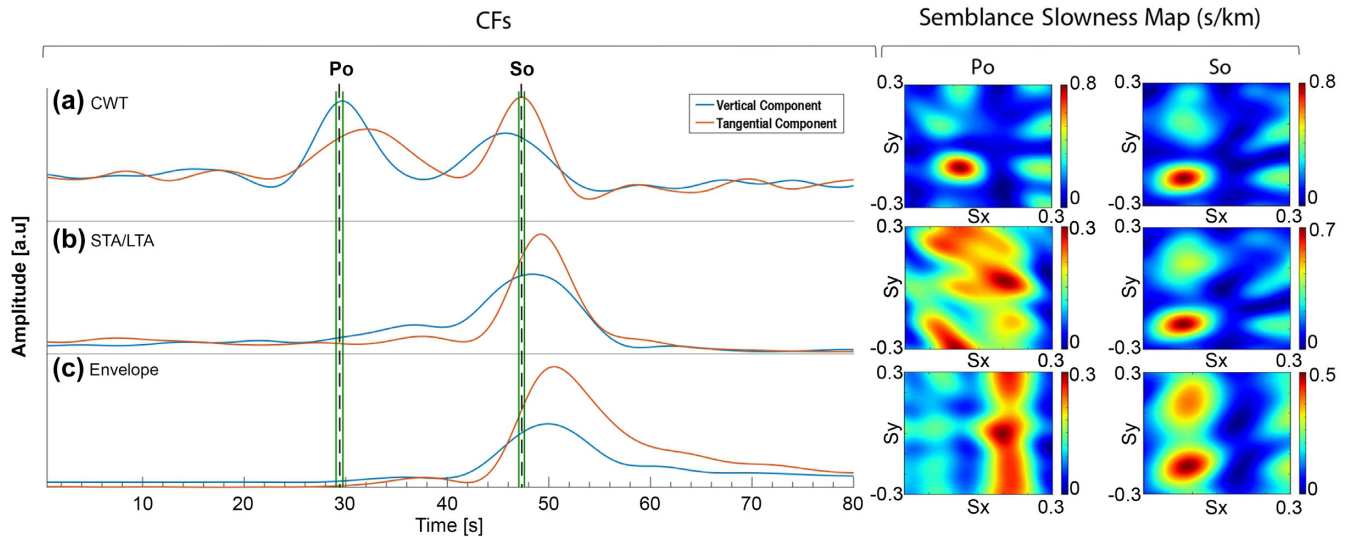
Figure 11. Earthquake T2 analysis with the new methodologies. (a) CWT-CFs beam for the vertical (blue line) and tangential (red line) component and the corresponding slowness map for the Po and So wave ($\omega o = 8$, frequency band 0.5–25 Hz). Po and So indicates the phase arrival times of the beamforming retrieved from the manual picks in the OBSs of the array. Green lines are the error bars ($\pm$ 0.3 s) associated with the manual picked Po and So beams. (b) The same as the first row for STA/LTA-CFs beam. (c) The same as (a) and (b), but for Envelope-CFs beam. In the AM, (a) and (b), a high-pass pre-filter was applied to the raw seismograms with a corner frequency, $f_c = 0.5$ Hz.

by the late Po-wave coda, mostly as a consequence of multiple scattering in the oceanic lithosphere. In this sense, if we want to avoid problems in the application of the AM implementation and boost its performance, we likely need to apply time correction terms to the estimated traveltimes.

In terms of computation time cost CWT has a slight disadvantage compared to the AM, although that disadvantage can be alleviated by pre-calculating a bank of atoms (in our case banks of Morlet wavelet atoms) before the implementation of CWT for the frequency band of interest. For example, the computation time ratios between the CWT and the AM methods for a 24 hr seismogram (sampling rate 50 samples s^{-1}) using a pre-calculated bank of atoms are

$$\frac{V_{cwt}}{V_{sta\_lta}} \approx 18 \tag{8}$$

$$\frac{V_{cwt}}{V_{envelope}} \approx 1.4 \tag{9}$$

where V_{cwt}, V_{sta_lta} and $V_{envelope}$ are the processing speeds of 24 hr data for the CWT, STA/LTA and envelope methods. Nevertheless, V_{cwt} for this example is approximately 1.6 s, which shows that the CWT methodology is also feasible for the analysis of large amounts of data sets.

An additional test has been carried out to analyze the possibilities of the CWT methodology as a detector for low SNR signals. We select the OBS06 vertical record of Earthquake T1 to compute the CWT (Fig. 12a) with a number of cycles varying in the range $[5 - 10]$ for the frequency band $[2 - 8]$ Hz. The seismogram has a relative emergent Po phase onset with a smaller amplitude than the So phase and it also has a significant long Po coda that partially masks the So onset.

The test starts with a gradual contamination of the signal adding white Gaussian noise from -85 up to -5 dB of the maximum power of the signal in steps of 5 dB (Fig. 12b). In parallel, the CFs are estimated through the CWT methodology in each iteration. Fig. 12(d) displays all CFs derived for each iteration highlighting

the CF (red line) retrieved with the maximum noise level (-5 dB of the maximum power of the signal). After the full contamination, the most obscured phase is the Po wave which is almost completely masked in the noise and the So onset is not distinguishable. In terms of the CFs' shape, the peak of CFs that corresponds to the So wave still preserves its shape but the maxima that corresponds to the Po onset is delayed with respect to the original Po CF maxima. The energy of the full signal is still detected in the scalogram after the noise addition, however some oscillations in the higher frequencies are partially hidden.

To sum up, the test gives an overview of the limit where the CFs lose their shapes and thus their time resolution, showing that the CWT methodology is robust enough to detect seismic signals in highly contaminated ambient noise.

Hereafter, we compare the epicentre locations obtained by the CWT method (E1) with the reference E2. In the first step, the epicentral distance between E1 and E2 is analysed and in a second step, the BAZ and slowness deviations between those locations.

Characteristically, earthquakes between Cape Saint Vincent and the array (T3, T5, T9 and T16) are well constrained being a good reference for the comparison with array locations. However, the locations around the Gorringe Bank and those off of the west coast of Morocco are more susceptible to large location errors. From the epicentre comparison (Fig. 7), we found small location differences for all of the epicentres except for Events T7 and T12 (Table 1, Dist 14.5 and 28.0 km, respectively). Both epicentre determinations (E1 and E2) are consistent, with a mean inter-epicentre distance of 12 km and a standard deviation of 6 km. Those results are reinforced by the overlap between the uncertainty ellipse associated with the location of the non-linear method (Table 1, L1 and L2) and the uncertainty of the array beam (beam from the center of the array toward the calculated BAZ and the width of the beam obtained through $\pm\Delta$BAZ, Table 1), with the exception of Earthquake T12 (high location errors).

The anomalous BAZ differences (*P*-wave maximum of 7° and *S*-wave maximum of 10°, Fig. 8) in the angular sector [60°–120°], may be explained by the poor quality of the earthquake locations in that
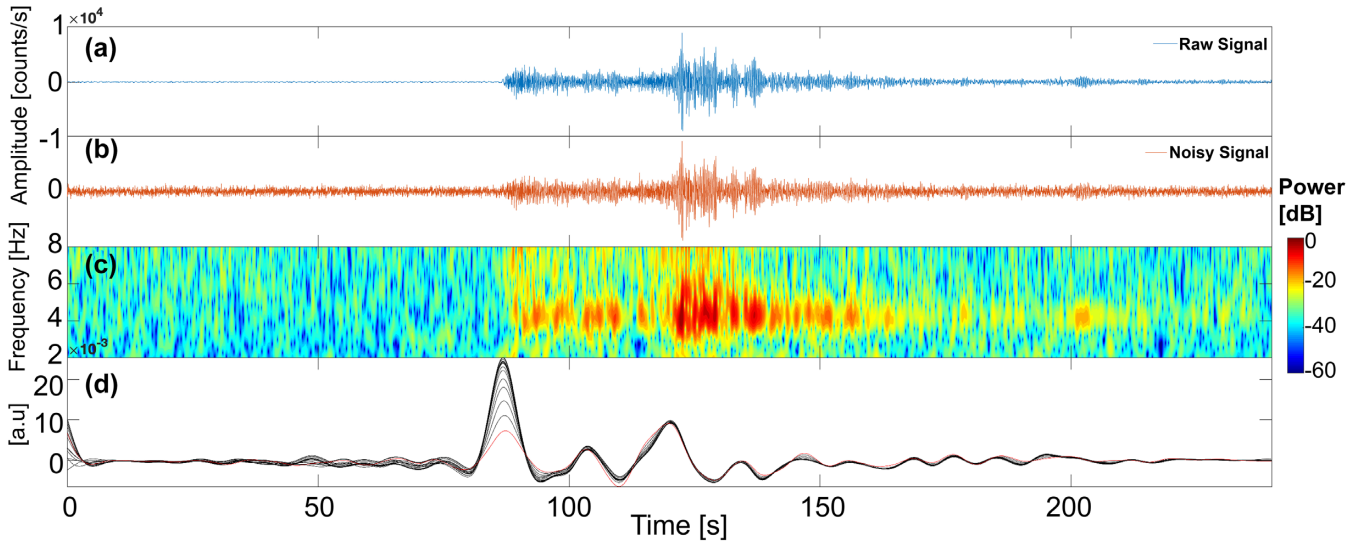
Figure 12. (a) Raw signal of the regional Earthquake T1 (Table 1). (b) Raw seismogram with additional white Gaussian noise (-5 dB of the maximum power of the signal). (c) Scalogram of the contaminated seismogram. (d) CFs calculated with the CWT methodology for white noise varying in amplitude from -85 up to -5 dB of the maximum power of the signal in steps of 0.5 dB.
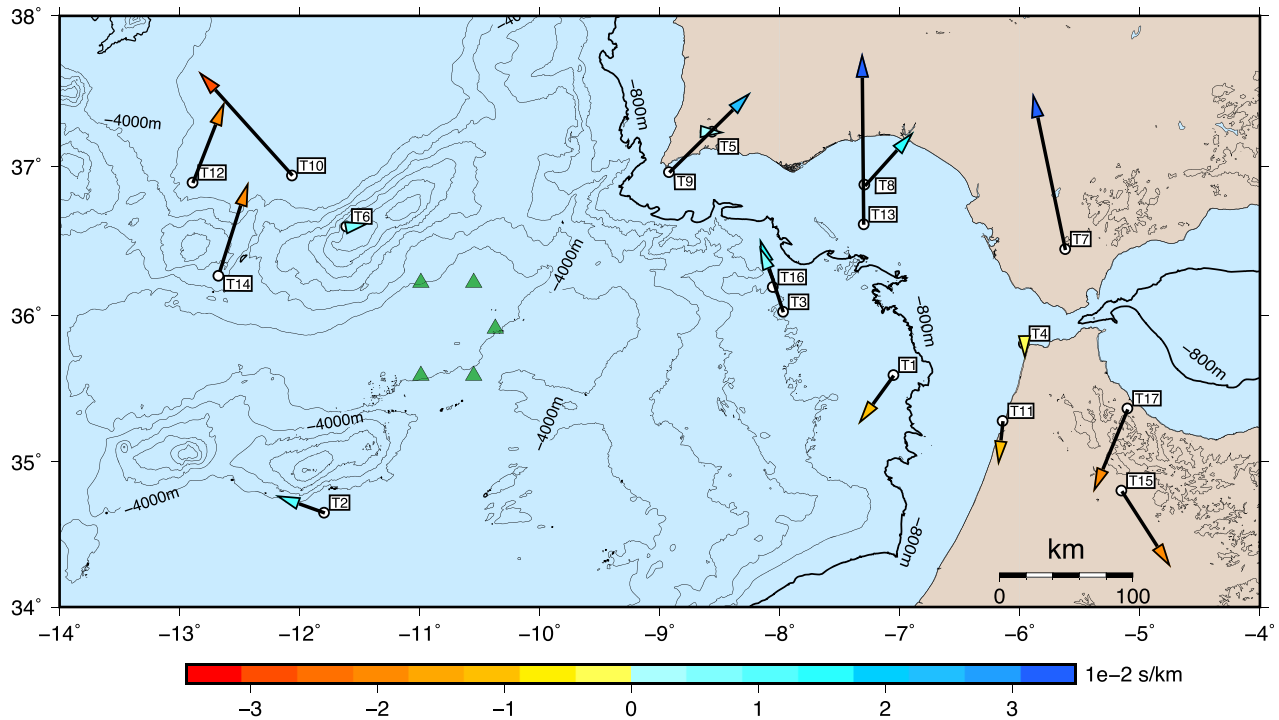
Figure 13. Slowness deviation. Arrows point from E2 to E1 locations and the head arrow colours highlight the slowness difference (S_p difference Table 1, difference between theoretical slowness from ray tracing using the Earth velocity 3-D model and estimated slowness from the CWT methodology of the *P* wave). The length of the arrows is proportional to the slowness deviation (i.e. see colour scale). The bathymetry isoline at 800 m depth is highlighted.

area. Even though a 3-D model was implemented to calculate the hypocentres, the lack of azimuth coverage with stations in the south yields a high latitude location error. In the other angular sector with high BAZ differences [270°–330°], the seismic waves come from the GB, which is a high-velocity crust-upper-mantle region both for *P* and *S* waves (González-Fernández *et al.* 2001). Moreover, the OBS array is placed in the HAP, which is characterized as a diffuse plate boundary (Jiménez-Munt *et al.* 2001; Palano *et al.* 2015) where sharp seismic wave velocity gradients may cause deviations in the

wave path; however such an analysis is beyond the scope of this paper.

Fig. 13 displays arrows pointing from E2 to E1 locations and the head arrow colours highlight the slowness difference, S_p (difference between empirical slowness and estimated slowness from the CWT methodology of the *P* wave). Here, we assess a remarkable odd symmetry, with slowness deviations that might be caused by the heterogeneous structure below the array (with high sediment thickness) and/or because of the complexity of the Eurasian-Nubian plate

boundary, which in this region shows sharp structural changes in the elastic properties of the lithosphere (Zitellini *et al.* 2009; Torne *et al.* 2015).

In summary, the results obtained from the epicentre locations show that the slowness vector can be calculated reliably with the new methodology. Considering the poor array performance of a large aperture array with a minimum number of sensors, the test estimations have reasonable errors.

6 CONCLUSIONS

The new methodology based on the CWT confirms that the slowness vector can be estimated in an array (land or ocean bottom stations array) with a small number of stations and waveforms with a low degree of similarity. Even though, in the highest ambient noise conditions such as marine ambient noise, the CWT can detect signals and extract the wave energy content to form the CFs. A faster alternative based on the STA/LTA and the envelope has also been explored for comparison (AM). Both methods have specific advantages regarding the estimation of the slowness vector, that is, the multiresolution time–frequency analysis flexibility and robustness of the CWT method and the speed and simplicity of the AM.

The applicability of the methodology has been tested with an OBS large-aperture sparse array in the HAP, a region with complex heterogeneities underneath the array. Despite the difficulties from pre-processing OBS data (clock synchronization and horizontal components orientation) and the poor array performance, it has been possible to estimate the slowness vector from regional phases and to derive epicentral locations with reasonable errors. From the BAZ differences, we underline the high values in a specific angular sector $[60°–120°]$. More data analysis will be required from extended periods to better understand the azimuth anisotropy of *P* and *S* waves in the GC.

REFERENCES

Allen, R., 1982. Automatic phase pickers: their present use and future prospects, *Bull. seism. Soc. Am.,* **72,** S225–S242.

Almendros, J., Ibáñez, J.M., Alguacil, G. & Del Pezzo, E., 1999. Array analysis using circular-wave-front geometry: an application to locate the nearby seismo-volcanic source, *Geophys. J. Int.,* **136,** 159–170.

Bayram, İ., 2013. An analytic wavelet transform with a flexible time-frequency covering, *IEEE Trans. Signal Process.,* **61,** 1131–1142.

Bear, L.K. & Pavlis, G.L., 1997. Estimation of slowness vectors and their uncertainties using multi-wavelet seismic array processing, *Bull. seism. Soc. Am.,* **87,** 755–769.

Behr, Y., Townend, J., Bowen, M., Carter, L., Gorman, R., Brooks, L. & Bannister, S., 2013. Source directionality of ambient seismic noise inferred from three-component beamforming, *J. geophys. Res.: Solid Earth,* **118,** 240–248.

Beyreuther, M., Barsch, R., Krischer, L., Megies, T., Behr, Y. & Wassermann, J., 2010. ObsPy: a Python toolbox for seismology, *Seismol. Res. Lett.,* **81,** 530–533.

Bruns, A., 2004. Fourier-, Hilbert-and wavelet-based signal analysis: are they really different approaches? *J. Neurosci. Methods,* **137,** 321–332.

Buforn, E., Bezzeghoud, M., Udias, A. & Pro, C., 2004. Seismic sources on the Iberia-African plate boundary and their tectonic implications., *Pure and Applied Geophysics,* **161**:623–646.

Cabieces, R., Buforn, E., Cesca, S & Pazos, A., 2020. Focal Parameters of Earthquakes Offshore Cape St. Vincent Using an Amphibious Network, *Pure Appl. Geophys,* **177**:1761–1780,.

Capon, J., 1969. High-resolution frequency-wavenumber spectrum analysis, *Proc. IEEE,* **57,** 1408–1418.

Carminati , E., Wortel, M., Spakman, W. & Sabadini, R., 1998. The role of slab detachment processes in the opening of the western–central Mediterranean basins: some geological and geophysical evidence., *Earth and Planetary Science Letters,* **160**(3-4):651–665.

Carpenter, E., 1965. An historical review of seismometer array development, *Proc. IEEE,* **53,** 1816–1821.

Cessaro, R.K., 1994. Sources of primary and secondary microseisms, *Bull. seism. Soc. Am.,* **84,** 142–148.

Collins, J., Vernon, F., Orcutt, J. & Stephen, R., 2002. Upper mantle structure beneath the Hawaiian swell: constraints from the ocean seismic network pilot experiment, *Geophys. Res. Lett.,* **29,** 17–11-17-14.

Dahm, T., Tilmann, F. & Morgan, J., 2006. Seismic broadband ocean-bottom data and noise observed with free-fall stations: experiences from long-term deployments in the North Atlantic and the Tyrrhenian Sea, *Bull. seism. Soc. Am.,* **96,** 647–664.

Daubechies, I. & Bates, B.J., 1992. *Ten Lectures on Wavelets*. ASA.

Doornbos, D., 1974. Seismic wave scattering near caustics: observations of PKKP precursors, *Nature,* **247,** 352–353.

Frankel, A., Hough, S., Friberg, P. & Busby, R., 1991. Observations of Loma Prieta aftershocks from a dense array in Sunnyvale, California, *Bull. seism. Soc. Am.,* **81,** 1900–1922.

Friedrich, A., Krueger, F. & Klinge, K., 1998. Ocean-generated microseismic noise located with the Gräfenberg array, *J. Seismol.,* **2,** 47–64.

Gal, M., Reading, A.M., Ellingsen, S., Gualtieri, L., Koper, K., Burlacu, R., Tkalčić, H. & Hemer, M., 2015. The frequency dependence and locations of short-period microseisms generated in the Southern Ocean and West Pacific, *J. geophys. Res.: Solid Earth,* **120,** 5764–5781.

Gharti, H.N., Oye, V., Roth, M. & Kühn, D., 2010. Automated microearthquake location using envelope stacking and robust global optimization Automated microearthquake location, *Geophysics,* **75,** MA27–MA46.

Gibbons, S.J., 2012. The applicability of incoherent array processing to IMS seismic arrays, *Pure appl. Geophys.,* **171,** 377–394.

Gibbons, S.J & Ringdal, F., 2012. Seismic monitoring of the North Korea nuclear test site using a multichannel correlation detector, *IEEE Trans. Geosci. Remote Sens.,* **50,** 1897–1909.

Gibbons, S.J., Ringdal, F. & Kværna, T., 2008. Detection and characterization of seismic phases using continuous spectral estimation on incoherent and partially coherent arrays, *Geophys. J. Int.,* **172,** 405–421.

Goldstein, P., Walter, W.R. & Zandt, G., 1992. Upper mantle structure beneath central Eurasia using a source array of nuclear explosions and waveforms at regional distances, *J. geophys. Res.: Solid Earth,* **97,** 14097–14113.

González-Fernández, A., Córdoba, D., Matias, L. & Torné, M., 2001. Seismic crustal structure in the Gulf of Cadiz (SW Iberian Peninsula), *Mar. Geophys. Res.,* **22,** 207–223.

Grandin, R., Borges, J.F., Bezzeghoud, M., Caldeira, B. & Carrilho, F., 2007. Simulations of strong ground motion in SW Iberia for the 1969 February 28 (M s = 8.0) and the 1755 November 1 (M~ 8.5) earthquakes–I. Velocity model, *Geophys. J. Int.,* **171,** 1144–1161.

Grevemeyer, I., Lange, D., Villinger, H., Custódio, S. & Matias, L., 2017. Seismotectonics of the Horseshoe Abyssal Plain and Gorringe Bank, eastern Atlantic Ocean: constraints from ocean bottom seismometer data, *J. geophys. Res.: Solid Earth,* **122,** 63–78.

Grigoli, F., Cesca, S., Vassallo, M. & Dahm, T., 2013. Automated seismic event location by travel-time stacking: an application to mining induced seismicity, *Seismol. Res. Lett.,* **84,** 666–677.

Grossmann, A., Kronland-Martinet, R. & Morlet, J., 1989. Reading and understanding continuous wavelet transforms, Wavelets, in *Time-Frequency Methods and Phase Space*. Springer, Berlin, Heidelberg, pp. 2–20.

Gutscher, M.-A., 2004. What caused the great Lisbon earthquake? , *Science,* **30,** 1247–1248.

Gutscher, M.-A., Malod , J., Rehault , J.-P., Contrucci , I., Klingelhoefer, F., Mendes-Victor, L. & Spakman, W., 2002. Evidence for active subduction beneath Gibraltar, *Geology,* **30,** 1071–1074.

Haney, M.M., Power, J., West, M. & Michaels, P., 2012. Causal instrument corrections for short-period and broadband seismometers, *Seismol. Res. Lett.,* **83,** 834–845.

Hannemann, K., Krüger, F. & Dahm, T., 2013. Measuring of clock drift rates and static time offsets of ocean bottom stations by means of ambient noise, *Geophys. J. Int.,* **196,** 1034–1042.

Ishii, M., Shearer, P.M., Houston, H. & Vidale, J.E., 2005. Extent, duration and speed of the 2004 Sumatra–Andaman earthquake imaged by the Hi-Net array, *Nature,* **435,** 933.

Jiménez-Munt, I., Fernàndez, M., Torne, M. & Bird, P., 2001. The transition from linear to diffuse plate boundary in the Azores–Gibraltar region: results from a thin-sheet model, *Earth planet. Sci. Lett.,* **192,** 175–189.

Kao, H. & Shan, S.J., 2007. Rapid identification of earthquake rupture plane using source-scanning algorithm, *Geophys. J. Int.,* **168,** 1011–1020.

Kennett, B. & Furumura, T., 2013. High-frequency Po/So guided waves in the oceanic lithosphere: I—long-distance propagation, *Geophys. J. Int.,* **195,** 1862–1877.

Kim, W.Y. & Richards, P.G., 2007. North Korean nuclear test: seismic discrimination low yield, *EOS, Trans. Am. geophys. Un.,* **88,** 158–161.

Kito, T. & Krüger, F., 2001. Heterogeneities in D” beneath the southwestern Pacific inferred from scattered and reflected P-waves, *Geophys. Res. Lett.,* **28,** 2545–2548.

Koper, K.D., Hutko, A.R., Lay, T., Ammon, C.J. & Kanamori, H., 2011. Frequency-dependent rupture process of the 2011 M w 9.0 Tohoku Earthquake: comparison of short-period P wave backprojection images and broadband seismic rupture models, *Earth Planets Space,* **63,** 16,.

,Krüger, F., Dahm, T. & Hannemann, K., 2020. Mapping of Eastern North Atlantic Ocean seismicity from Po/So observations at a mid-aperture seismological broad-band deep sea array, *Geophysical Journal International,* **221**(2), 1055–1080.

Krüger, F. & Ohrnberger, M., 2005. Tracking the rupture of the M w = 9.3 Sumatra earthquake over 1,150 km at teleseismic distance, *Nature,* **435,** 937–939,.

Krüger, F., Weber, M., Scherbaum, F. & Schlittenhardt, J., 1993. Double beam analysis of anomalies in the core-mantle boundary region, *Geophys. Res. Lett.,* **20,** 1475–1478.

Kumar, P. & Foufoula-Georgiou, E., 1997. Wavelet analysis for geophysical applications, *Rev. Geophys.,* **35,** 385–412.

Kværna, T. & Ringdal, F., 2013. Detection capability of the seismic network of the International Monitoring System for the Comprehensive Nuclear-Test-Ban Treaty, *Bull. seism. Soc. Am.,* **103,** 759–772.

Le, B.M., Yang, T., Chen, Y.J. & Yao, H., 2018. Correction of OBS clock errors using Scholte waves retrieved from cross-correlating hydrophone recordings, *Geophys. J. Int.,* **212,** 891–899.

Lomax, A., Michelini, A. & Curtis, A., 2009. Earthquake location, direct, global-search methods, in *Encyclopedia of Complexity and Systems Science,* Springer, Meyers, Robert A., pp. 2449–2473,.

Lomax, A., Zollo, A., Capuano, P. & Virieux, J., 2001. Precise, absolute earthquake location under Somma–Vesuvius volcano using a new three-dimensional velocity model, *Geophys. J. Int.,* **146,** 313–331.

Mallat, S., 2009. *A Wavelet Tour of Signal Processing,* Third ed. Academic Press.

Mallick, S. & Frazer, L., 1990. Po/So synthetics for a variety of oceanic models and their implications for the structure of the oceanic lithosphere, *Geophys. J. Int.,* **100,** 235–253.

Nawab, S., Dowla, F. & Lacoss, R., 1985. Direction determination of wide-band signals, *IEEE Trans. Acoust. Speech Signal Process.,* **33,** 1114–1122.

Oppenheim, A.V. & Schafer, R.W., 2010. *Discrete-Time Signal Processing,* 3rd ed. Pearson, Upper Saddle River.

Palano, M., González, P.J. & Fernández, J., 2015. The Diffuse Plate boundary of Nubia and Iberia in the Western Mediterranean: crustal deformation evidence for viscous coupling and fragmented lithosphere, *Earth planet. Sci. Lett.,* **430,** 439–447.

Platt, J., Whitehouse, M., Kelley, S., Carter, A. & Hollick, L., 2003. Simultaneous extensional exhumation across the Alboran Basin: implications for the causes of late orogenic extension, *Geology,* **31,** 251–254.

Pro, C., Bufforn, E., Bezzeghoud, M. & Udías, A., 2013. The earthquakes of 29 July 2003, 12 February 2007, and 17 December 2009 in the region of Cape Saint Vincent (SW Iberia) and their relation with the 1755 Lisbon earthquake., *Tectonophysics,* **583,** 16–27.

Reading, A.M., Koper, K.D., Gal, M., Graham, L.S., Tkalčić, H. & Hemer, M.A., 2014. Dominant seismic noise sources in the Southern Ocean and West Pacific, 2000–2012, recorded at the Warramunga Seismic Array, Australia, *Geophys. Res. Lett.,* **41,** 3455–3463.

Ringdal, F., Husebye, E., Dahle, A. & Beauchamp, K., 1975. *P-Wave Envelope Representation in Event Detection Using Array Data.* Nordhoff-Leiden, The Netherlands, pp. 353–372.

Rioul, O. & Flandrin, P., 1992. Time-scale energy distributions: A general class extending wavelet transforms., *IEEE Transactions on Signal Processing,* **40(7)**:1746–1757.

Rost, S. & Thomas, C., 2002. Array seismology: methods and applications, *Rev. Geophys.,* **40,** 2–1-2-27.

Rost, S. & Thomas, C., 2009. Improving seismic resolution through array processing techniques, *Surv. Geophys.,* **30,** 271–299.

Ruigrok, E., Gibbons, S. & Wapenaar, K., 2017. Cross-correlation beamforming, *J. Seismol.,* **21,** 495–508.

Sallarès,, V., Martínez-Loriente, S., Prada, M., Gràcia, E., Ranero, C., Gtuscher, M.A., Bartolome, R., Gailler, A., Dañobeitia, J.J. & Zitellini, N., 2013. Seismic evidence of exhumed mantle rock basement at the Gorringe Bank and the adjacent Horseshoe and Tagus abyssal plains (SW Iberia), *Earth and Planetary Science Letters,* **365,** 120–131,.

Scherbaum, F., 2001. *Of Poles and Zeros: Fundamentals of Digital Seismology*. Springer Science & Business Media.

Schweitzer, J., Fyen, J., Mykkeltveit, S., Gibbons, S., Pirli, M., Kühn, D. & Kvaerna, T., 2012. Seismic Arrays. - In: Bormann, P. (Ed.), *New Manual of Seismological Observatory Practice 2 (NMSOP-2), Potsdam : Deutsches GeoForschungsZentrum GFZ,* **Vol 1,** 1–80,.

Selby, N.D., 2010. Relative locations of the October 2006 and May 2009 DPRK announced nuclear tests using international monitoring system seismometer arrays, *Bull. seism. Soc. Am.,* **100,** 1779–1784.

Shiobara, H., Nakanishi, A., Shimamura, H., Mjelde, R., Kanazawa, T. & Berg, E.W., 1997. Precise positioning of ocean bottom seismometer by using acoustic transponder and CTD, *Mar. Geophys. Res.,* **19,** 199–209.

Shito, A., Suetsugu, D., Furumura, T., Sugioka, H. & Ito, A., 2013. Small-scale heterogeneities in the oceanic lithosphere inferred from guided waves, *Geophys. Res. Lett.,* **40,** 1708–1712.

Solares, J.M. & Arroyo, A.L., 2004. The great historical 1755 earthquake. Effects and damage in Spain, *Journal of Seismology,* **8**:275–294.

Stachnik, J., Sheehan, A.F., Zietlow, D., Yang, Z., Collins, J. & Ferris, A., 2012. Determination of New Zealand ocean bottom seismometer orientation via Rayleigh-wave polarization, *Seismol. Res. Lett.,* **83,** 704–713.

Stähler, S.C. *et al.*, 2016. Preliminary performance report of the RHUM-RUM ocean bottom seismometer network around La Réunion, western Indian Ocean, *Adv. Geosci.,* **41,** 43–63.

Tilmann, F.J. & Dahm, T., 2008. Constraints on crustal and mantle structure of the oceanic plate south of Iceland from ocean bottom recorded Rayleigh waves, *Tectonophysics,* **447,** 66–79.

Torne, M., Fernàndez, M., Vergés, J., Ayala, C., Salas, M.C., Jimenez-Munt, I., Buffett, G.G. & Díaz, J., 2015. Crust and mantle lithospheric structure of the Iberian Peninsula deduced from potential field modeling and thermal analysis, *Tectonophysics,* **663,** 419–433.

Trnkoczy, A., 2012. Understanding and parameter setting of STA/LTA trigger algorithm. - In: Bormann, P. (Ed.), *New Manual of Seismological Observatory Practice 2 (NMSOP-2),* **Vol 2,** 1–20,.

Weber, M., Davis, J., Thomas, C., Krüger, F., Scherbaum, F., Schlittenhardt, J. & Körnig, M., 1996. The structure of the lowermost mantle as determined from using seismic arrays, *Seismic Modeling of the Earth's Structure,* Instit. Naz. di Geophys, Boschi, E., Ekström, G. & Morelli, A., 399–442.

Wessel, P., Smith, W.H., Scharroo, R., Luis, J. & Wobbe, F., 2013. Generic mapping tools: improved version released, *EOS, Trans. Am. geophys. Un.,* **94,** 409–410.

Zha, Y., Webb, S.C. & Menke, W., 2013. Determining the orientations of ocean bottom seismometers using ambient noise correlation, *Geophys. Res. Lett.,* **40,** 3585–3590.

Zitellini, N. *et al.*, 2009. The quest for the Africa–Eurasia plate boundary west of the Strait of Gibraltar, *Earth planet. Sci. Lett.,* **280,** 13–50.

SUPPORTING INFORMATION

Supplementary data are available at *GJI* online.

Figure S1. The red line is the reference build from the stack of all daily NCCFs, while the blue line is an example of NCCF reconstructed between the OBS01 and the station PVAQ. δ_{stat}, initial correction is applied to the reference point in order to achieve an absolute clock correction. The blue boxes are the time window on the Rayleigh wave. It was estimated $4.0\ \mathrm{km\,s^{-1}}$ to start the windowing over the surface wave.

Figure S2. Comparison between the reference (OBS01−0BS02) build from a linear stack (upper panel, red line) and the ts-PWS (Ventosa *et al.* 2017, lower panel, blue line). The blue line enhances the predominant periods of the signal.

Figure S3. Curve fitting of the daily time difference OBS02. The upper panel black dots are the results of the cross-correlation between the reference of the OBS02 and land stations (South Portugal,

Fig. 7) NCCFs, the blue line is the curve fit and the red dashed line is the confidence bound 95 per cent. The lower panel displays the residual fit plot between the curve fitting and the results of the cross-correlations.

Figure S4. Horizontal component orientation from the Chile earthquake in 2015 September 16 (M_w 8.3). (a)–(c) are the vertical and horizontal components respectively of the OBS05. Part (d) shows bandpass filtered [0.01–0.06] Hz of the earthquake, blue represents the radial component and the red line the Hilbert transform of the vertical component (Correlation 0.92). Part (e) is an example of polar plot orientation OBS05, in which radius and colour are directly related to normalized correlation. The red line is the azimuth horizontal orientation mean value after the culling of the orientations results and the dashed red line plots is the standard deviation σ.

Figure S5. Earthquake T13, BB-FK analysis. CWT method upper panels, (a) Semblance $S(f,k)$. (b) $P(f,k)$. (c) and (d) temporal representation of the BAZ and slowness in accordance with the maximum $S(f,k)$. Lower panels: left, Po wave slowness map, and right, So wave slowness map.

Figure S6. (a) Seismogram of Earthquake T1 recorded on the vertical component of OBS06. (b) Scalogram computed with number of cycles equal to 5. (c) scalogram computed with number of cycles equal to 16. (d) Scalogram computed with number of cycles varying from 5 to 16 in the frequency band 2–12 Hz.

Figure S7. (a) A bank of atoms generated with constant number of cycles set to 6. (b) A bank of atoms generated increasing the number of cycles from 6 to 10.

Table S1. Fit results, first column is the skew of the OBSs at the recovery.

Table S2. Horizontal orientation results. Statistics applied after discarding correlation values < 0.4 and mean values from orientations inside 2σ.

Please note: Oxford University Press is not responsible for the content or functionality of any supporting materials supplied by the authors. Any queries (other than missing material) should be directed to the corresponding author for the paper.